

High Strain Rate Deformation Behavior and Recrystallization of Alloy 718



MARIE ANNA MORETTI, BISWAJIT DALAI, PAUL ÅKERSTRÖM,
CORINNE ARVIEU, DIMITRI JACQUIN, ERIC LACOSTE,
and LARS-ERIK LINDGREN

To study the deformation behavior and recrystallization of alloy 718 in annealed and aged state, compression tests were performed using Split-Hopkinson pressure bar (SHPB) at high strain rates (1000 to 3000 s⁻¹), for temperatures between 20 °C and 1100 °C (293 K to 1373 K). Optical microscope (OM) and electron back-scatter diffraction (EBSD) technique were employed to characterize the microstructural evolution of the alloy. The stress–strain curves show that the flow stress level decreases with increasing temperature and decreasing strain rate. In addition, up to 1000 °C, the aged material presents higher strength and is more resistant to deformation than the annealed one, with a yield strength around 200 MPa higher. For both states, dynamic and meta-dynamic recrystallization occurred when the material is deformed at 1000 °C and 1100 °C, leading to a refinement of the microstructure. As necklace structures were identified, discontinuous recrystallization is considered to be the main recrystallization mechanism. The recrystallization kinetics is faster for higher temperatures, as the fraction of recrystallized grains is higher and the average recrystallized grain size is larger after deformation at 1100 °C than after deformation at 1000 °C.

<https://doi.org/10.1007/s11661-021-06463-7>
© The Author(s) 2021

I. INTRODUCTION

ALLOY 718 is a nickel-chromium superalloy. It was developed in the 1960s and it is, nowadays, one of the most widely used superalloys due to its high strength, high corrosion resistance and good mechanical properties at high temperature. It also presents good fatigue, creep and wear resistance. It is used mainly in the aerospace and oil industries, for instance in the hot parts of gas turbine engines. Alloy 718 is a precipitate hardening alloy with a face-centred cubic Ni-Cr matrix, the γ phase. Two precipitates contribute to its strength: the γ' phase (Ni₃(Al,Ti)), which is face-centred cubic and spherical or cuboid, and the γ'' phase (Ni₃Nb(Ti,Al)), which is body-centred tetragonal and disc-shaped. The γ'' precipitates are usually considered as the main hardening precipitates in this alloy.

During hot working, metallic materials can undergo recrystallization, which corresponds to the replacement of deformed grains by a new defect-free grain structure by formation and migration of high angle boundaries (HABs).^[1] It was observed that recrystallization takes place in alloy 718 and other Ni-based alloys during manufacturing processes, for example during hot forging,^[2,3] friction welding^[4,5] and machining.^[6–8]

The deformation behavior of alloy 718 at low strain rate (below 1 s⁻¹) was extensively investigated for a wide range of temperatures. These studies showed and characterized the occurrence of dynamic recrystallization at high temperatures (above 900 °C) in this alloy.^[9–17] Iturbe *et al.*^[18] investigated the behavior of alloy 718 for medium strain rates (from 1 to 100 s⁻¹) and they concluded that dynamic recrystallization also takes place above 900 °C for these strain rates. Studies on the deformation behavior of alloy 718 at high strain rate (above 1000 s⁻¹) focused on temperatures up to 800 °C and thus did not report any recrystallization.^[19–24] Johansson *et al.*^[25] reported that dynamic recrystallization occurs in shear bands forming during both metal cutting and shear tests, due to local adiabatic heating and strain localization.

This research work is part of a project which aims to simulate the deformation of alloy 718 during high temperature and high strain rate manufacturing processes. The objective of the current study is to

MARIE ANNA MORETTI, BISWAJIT DALAI, PAUL ÅKERSTRÖM, and LARS-ERIK LINDGREN are with the Department of Engineering Sciences and Mathematics, Luleå University of Technology, 97187 Luleå, Sweden. Contact e-mail: marie.anna.moretti@ltu.se CORINNE ARVIEU, DIMITRI JACQUIN, and ERIC LACOSTE are with the CNRS, Arts et Metiers Institute of Technology, Bordeaux INP, INRAE, I2M Bordeaux, University of Bordeaux, 33400, Talence, France.

Manuscript submitted April 7, 2021; accepted August 26, 2021
Article published online October 10, 2021

characterize the deformation behavior and recrystallization of alloy 718 for both high strain rates (1000 to 3000 s^{-1}) and high temperatures (up to 1100 °C), conditions that were not tackled by previously published research on this alloy.

II. MATERIAL AND METHODS

A. Material

In this study, alloy 718 was used in two different states: annealed and aged. As hardening precipitates γ'' form during aging,^[26] aged alloy 718 presents higher strength and hardness but lower ductility than the annealed material.^[27] Thus, both states are used in the industry, depending on the application.^[28,29] For this work, two bars of alloy 718 were provided by Sandvik Coromant with a diameter of 9.5 mm. One of the bars was used in its as-received annealed state and the other was aged according to the aging treatment presented in Figure 1. It consisted of solution heat-treatment for one hour at 954 °C, cooling to 593 °C in one hour and then cooling to room temperature, followed by aging for 5 hours at 760 °C, cooling to 649 °C in two hours, holding at this temperature for one hour before cooling to room temperature. Cylindrical samples were cut from both bars with a length of 4 mm and a diameter of 9.5 mm.

B. Mechanical Tests

Compression tests at high strain rate on alloy 718 samples were performed using Split-Hopkinson pressure bar (SHPB) coupled with an induction heating system,^[30] as shown in Figure 2. The tests were conducted at 20 °C, 400 °C, 800 °C, 1000 °C and 1100 °C, for strain rates between 1000 and 3000 s^{-1} . For each test, a K-type thermocouple was welded on the curved side of the sample to measure the temperature and the sample was placed in an induction coil between the two Split-Hopkinson bars. The sample was heated to the selected temperature and solenoids were used to push the bars in contact with the sample just an instant before the arrival of the first compressive wave, thus avoiding heat dissipation in the bars. Strain gauges on both bars

allowed to measure the incident, transmitted and reflected strains. After the test, the samples were quenched in cold water. Figure 3 shows the temperature of the sample over the entire testing procedure, including heating, compression and cooling, when the aimed deformation temperature was set to 1000 °C.

The stress σ_s , strain rate $\dot{\epsilon}_s$ and strain ϵ_s in the sample were calculated from the acquired data according to the classic Split-Hopkinson theory,^[31] assuming that the specimen is in force equilibrium and that it deforms uniformly:

$$\sigma_s = \frac{AE\epsilon_t}{A_s}, \quad [1]$$

$$\dot{\epsilon}_s = \frac{2C_b\epsilon_r}{L_s}, \quad [2]$$

$$\epsilon_s = \int_0^t \dot{\epsilon}_s dt = \frac{2C_b}{L_s} \int_0^t \epsilon_r dt, \quad [3]$$

where A and E are the cross-sectional area and the Young's modulus of the Split-Hopkinson bars, respectively; A_s and L_s are the instantaneous cross-sectional area and length of the specimen, respectively; C_b is the longitudinal wave speed in the bars; ϵ_i , ϵ_t and $\epsilon_r = \epsilon_t - \epsilon_i$, are the incident, transmitted and reflected strains in the bars, respectively.

The curves presented in this paper were smoothed using a moving average algorithm. The strain rate in the sample was not constant throughout the test, thus the strain rates indicated in this paper correspond to an average of the actual strain rate over the duration of the compressive test. Each test was repeated two to three times and the variation in flow stress was less than 10 pct.

C. Microstructural Characterization

Microstructural characterization using optical microscope (OM) and scanning electron microscope (SEM) was performed on the initial material, as well as on several samples deformed with the SHPB at 800, 1000 and 1100 °C. For each sample, the surface perpendicular to the compression direction was observed and the images presented in this study were taken at the center of the samples. All the samples were hot mounted in hard resin (Bakelite with carbon filler), ground with SiC papers and polished with a diamond paste (3 μm and 1 μm).

For the optical microscopy, the samples were polished with 0.05 μm colloidal silica for a few minutes and then electro-etched with a solution of 10 g of oxalic acid and 100 mL of distilled water for 10 to 15 seconds at 6 V. The samples were observed with an Olympus PMG 3 optical microscope equipped with a numerical camera and Stream software and with a LEICA DMI 5000 optical microscope with MultiFocus software.

For scanning electron microscopy, the samples were polished with 0.05 μm colloidal silica for 30 to 45 minutes. Observations were made with an FEI-Nova

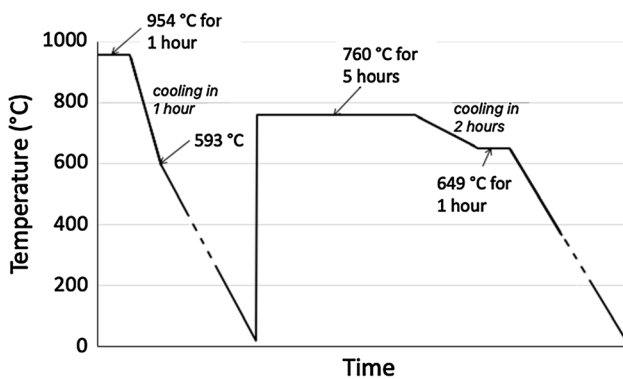


Fig. 1—Temperature history of the present aged alloy 718.

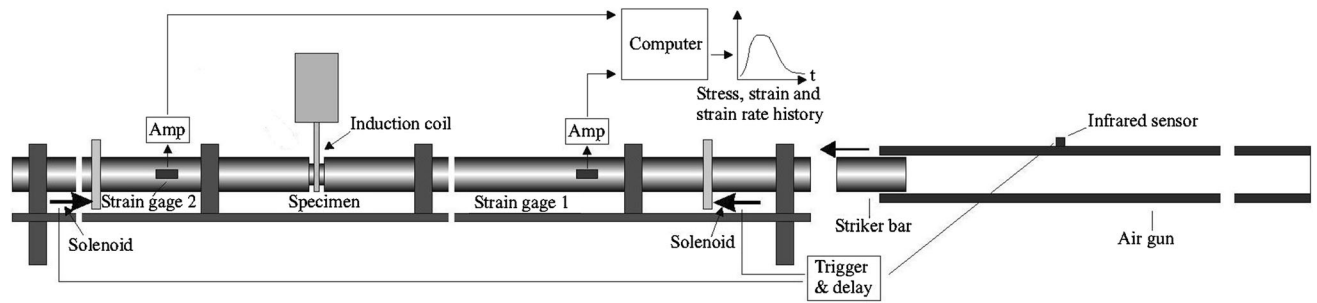


Fig. 2—Split-Hopkinson pressure bar set-up (adapted from^[30]).

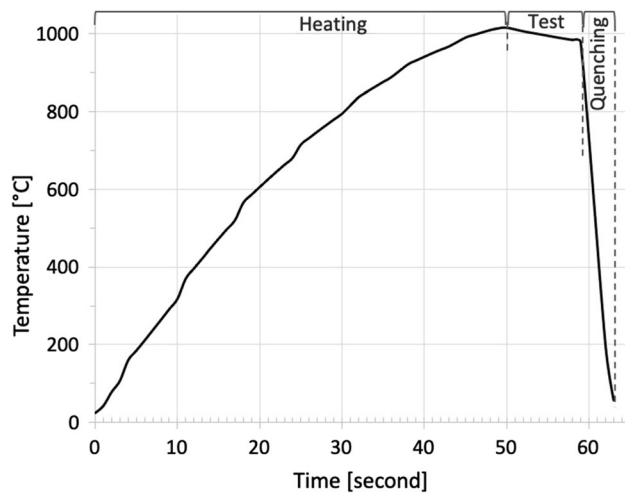


Fig. 3—Evolution of the temperature for a sample deformed at 1000 °C (measured with a thermocouple).

NNS 450 SEM coupled with an EDS-BRUKER detector for energy-dispersive X-ray spectroscopy (EDS) and with an EBSD-EDAX detector for electron backscatter diffraction (EBSD) analysis. The beam voltage for both EDS and EBSD was set to 20 kV. All the EBSD scans were taken in view field area $277 \times 277 \mu\text{m}^2$ with a step size of $0.5 \mu\text{m}$. OIM software was used for analyzing the EBSD images, by defining a “grain” with grain tolerance angle of 15 deg, minimum grain size of 10 pixels and the minimum confidence index (CI) of 0.1.

III. RESULTS

A. Initial Microstructure

The as-received material was characterized using OM and SEM. The initial microstructure, shown in Figure 4, is equiaxed with an average grain size close to $15 \mu\text{m}$, for both states. The chemical composition in weight percent (wt pct) of the as-received material obtained from the EDS analysis is shown in Table I. It is imperative to note that EDS works as best as only “semi-quantitative” in capability,^[32] and therefore, the chemical composition presented here need to be viewed in a semi-quantitative light without more standardization. Variations of less than ± 3 pct in nickel, chromium and iron contents indicate that the composition of the alloy used in the

current study is consistent with the recommendations for a standard alloy 718.^[28]

B. Stress–Strain Behavior

The stress–strain curves of alloy 718 in both annealed and aged states for temperatures between 20 and 1100 °C are shown in Figure 5. It is observed that the flow stress level decreases with increasing temperature. This is an expected result considering that dislocations become more mobile when the temperature increases, due to diffusion of atoms, as well as possible dissolution of the precipitates and other thermal effects. Similarly, the strain hardening, which is related to the slope of the flow stress curve in the plastic region, decreases with increasing temperature, as thermally activated mechanisms make movement and annihilation of dislocations easier. For the annealed material, Figure 5(a), it is also observed that the temperature sensitivity decreases with increasing temperature, the flow stress level being similar for deformations at 1000 °C and 1100 °C. This phenomenon was also reported by Lee *et al.*^[19,20] in the high strain rate domain but at lower temperatures.

The effect of strain rate was also investigated for the annealed and aged materials. In both cases, similar observations were made and the results for the annealed state are presented in Figure 6. As a general trend, the flow stress level increases with increasing strain rate. This is explained by a lack of time for thermal activation during deformation at high strain rate, thus the density of dislocations increases and they impede each other’s movements. However, the strain rate sensitivity, which can be obtained by $m = (\log(\sigma_2) - \log(\sigma_1)) / (\log(\dot{\epsilon}_2) - \log(\dot{\epsilon}_1))$,^[33,34] decreases with increasing temperature. On Figure 6, for a strain of 0.1, m is equal to 0.38 at 20 °C and to 0.13 at 800 °C, and at 1100 °C, the effect of strain rate is negligible. This result corroborates the observations made by Wang *et al.*^[22] and Lee *et al.*^[19] in the high strain rate domain (10^3 to 10^4 s^{-1}), who explain that strain rate hardening is restrained by thermal softening at high temperatures.

When comparing the two states of alloy 718, as shown in Figure 7, the yield stress and the flow stress level are higher for the aged material. The aging process allows hardening precipitates to form in large amount within the material, resulting in greater hardness and strength compared to the annealed state.^[27] On the other hand,

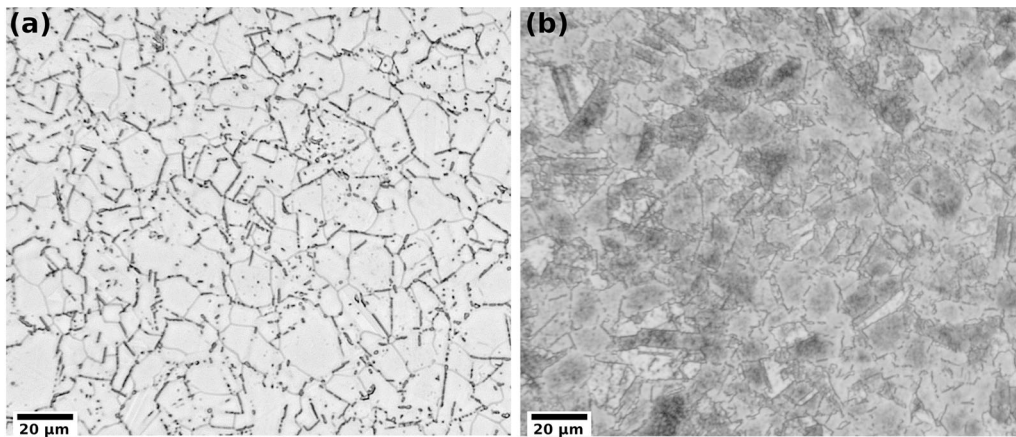


Fig. 4—Optical micrographs of the initial microstructure of the alloy 718 samples (a) in annealed (b) in aged state.

elongation is larger for the annealed material, which is more ductile. Nevertheless, the difference in flow stress between the annealed and aged states decreases at 1000 °C and disappears at 1100 °C. Above the homogenisation temperature, around 950 °C, the precipitates start to dissolve and the aged material loses its hardening properties.^[18,35] In addition, the aged material exhibits less hardening than the annealed one, as it has also been observed by other authors.^[36,37]

C. Microstructure Analysis

Characterization of the deformed material was performed using OM and EBSD to gather information about the microstructural mechanisms taking place during deformation. The effect of deformation temperature on alloy 718 microstructure in annealed and aged states is shown in Figures 8 and 9, respectively. The standard stereographic triangle for the color coding of the inverse pole figure (IPF) maps shown in the current study represents the crystal direction along the axis perpendicular to the plane of the maps. As previously mentioned, the initial grain size is approximately 15 μm, and the EBSD analysis reveals that many twin boundaries can be found in the initial state, as indicated by the black arrows in Figures 8 and 9. In the material deformed at 800 °C, the grains have the same average size as the initial material (around 15 μm) and twin boundaries are also present in the material. For higher deformation temperatures, 1000 °C and 1100 °C, a significant transformation of the microstructure was observed. At 1000 °C, the grain size is non homogeneous, containing small grains between 1 and 6 μm and large grains with an average size of 15 μm. It can also be noted that very few twin boundaries are observed at this temperature. At 1100 °C, the grain size is relatively homogeneous. Depending on the strain rate, the average

grain size is in the range of 5 to 9 μm. For this temperature, there are also very few twin boundaries.

It is known that dislocations in a material generate local variations in the lattice orientation. Thus, measurements of such misorientations give evidence for plastic deformation.^[38] In OIM analysis, the grain orientation spread (GOS) corresponds to a calculation of local misorientations. Figures 10 and 11 present the GOS maps for the same areas as the ones in Figures 8 and 9, respectively. Blue grains correspond to grains with a low GOS value (between 0 and 2), meaning that they are undeformed or recrystallized, depending on their deformation history. Green and red grains correspond to grains with a high GOS value (above 2), which means that there is a high number of dislocations in those grains. Thus, they are described as deformed (GOS between 2 and 5, green grains) or heavily deformed (GOS between 5 and 15, red grains). It can be noted that the black spots correspond to zones which are not defined as grains, according to the settings mentioned in Section II–C. Figure 12 summarizes the information of the GOS maps in a histogram, for the annealed and aged material. It can be observed that the initial material contains approximately 80 pct of undeformed grains for both states. For a deformation temperature of 800 °C, the annealed material appears to be highly deformed, with roughly 55 pct of the grains having a GOS value above 2, but in the aged material, the proportion of deformed grains is similar to the initial state, close to 20 pct. As mentioned in Section III–B, the aged material is harder and more resistant to deformation compared to the annealed state. The material deformed at 1000 °C presents, in both states, approximately 70 pct of undeformed or recrystallized grains and 30 pct of deformed grains. In this non-homogeneous microstructure, the largest grains are all deformed or heavily deformed. After deformation at 1100 °C, the material is mostly composed of recrystallized grains (approximately 80 pct).

Table I. Chemical Composition of Alloy 718 Material Used in This Study Measured by EDS Analysis

Element	Ni	Fe	Cr	Nb	Mo	Ti	Al
Wt Pct	49.62 ± 1.35	17.58 ± 0.49	17.18 ± 0.49	4.75 ± 0.20	2.58 ± 0.12	1.08 ± 0.06	0.43 ± 0.05

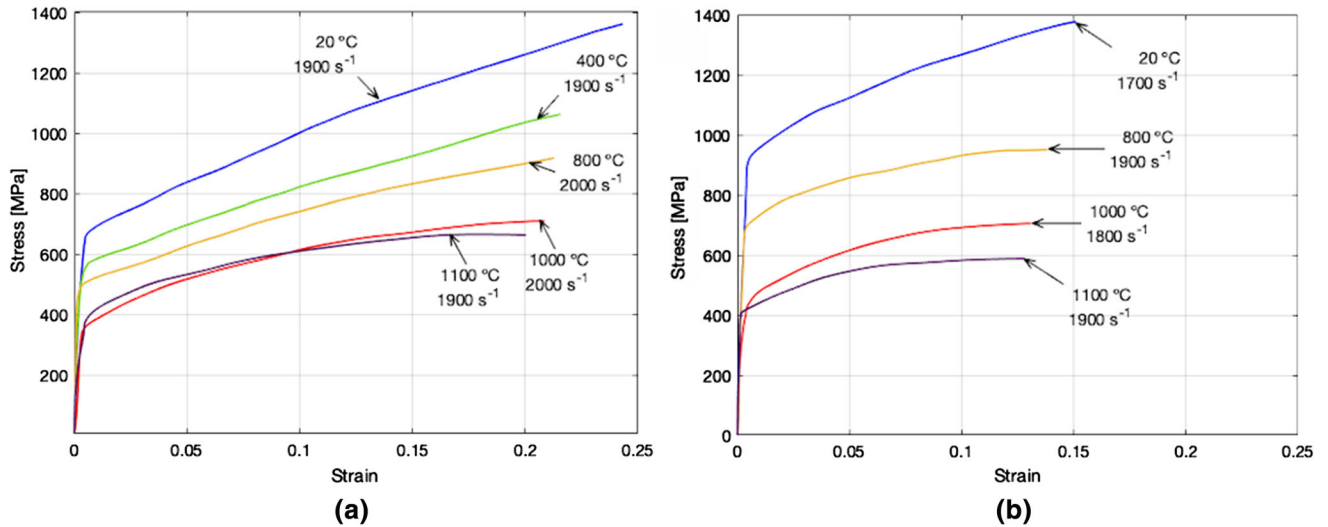


Fig. 5—True stress–strain curves of alloy 718 (a) in annealed state (b) in aged state for different temperatures.

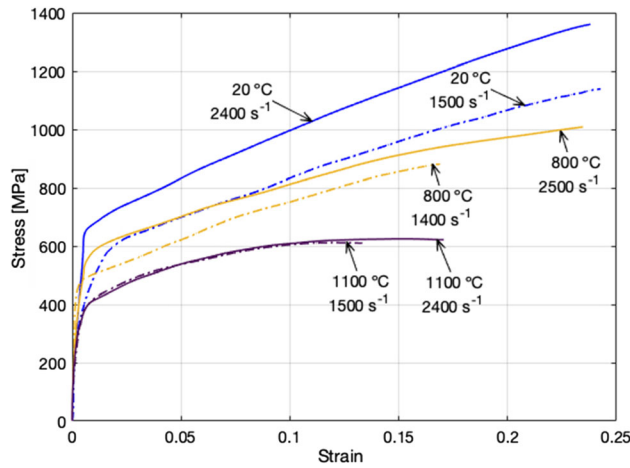


Fig. 6—True stress–strain curves of alloy 718 in annealed state for different strain rates at 20 °C, 800 °C and 1100 °C.

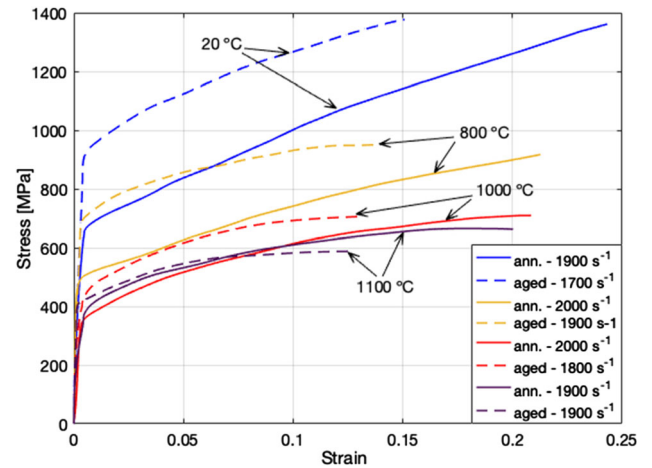


Fig. 7—True stress–strain curves of alloy 718 in annealed state (continuous curves) and aged state (dashed curves) for different temperatures.

IV. DISCUSSION

A. Recrystallization Process

Recrystallization phenomenon is usually divided into static recrystallization (SRX) and dynamic recrystallization (DRX). The first one takes place during annealing, whereas the second one is defined as a mechanism occurring during deformation. Meta-dynamic recrystallization (MDRX), which can follow the dynamic one, corresponds to a coarsening of the newly-formed recrystallized grains.^[39] In the current study, the compressive wave going through the sample has a duration

of around 200 μ s, making it unlikely for the recrystallized microstructure to form only during this short period of time. It is instead assumed that the recrystallization starts during the deformation and continues after it, before quenching.^[40] Thus, the studied phenomenon in this work corresponds to dynamic and meta-dynamic recrystallization. As it is not possible to distinguish the contribution of DRX and MDRX using standard EBSD data,^[41] the term “recrystallization” in this study refers to both dynamic and meta-dynamic recrystallization.

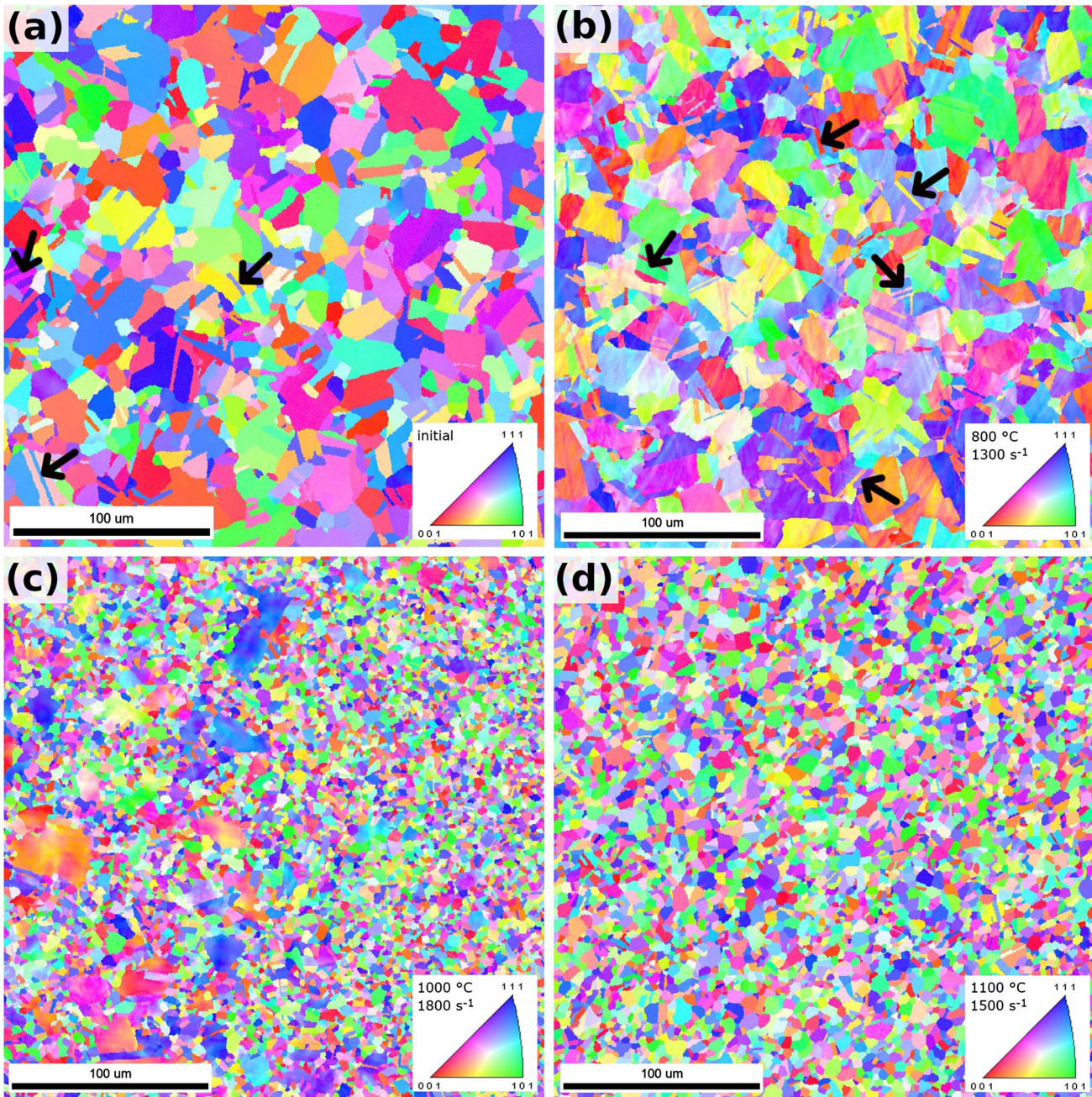


Fig. 8—Inverse Pole Figures (IPF) obtained by EBSD analysis of alloy 718 in annealed state (a) initial material (b) deformed at 800 °C (c) deformed at 1000 °C (d) deformed at 1100 °C (strain rate between 1300 s⁻¹ and 1800 s⁻¹)—black arrows indicate twins (Color figure online).

Two types of dynamic recrystallization mechanisms can be differentiated: discontinuous dynamic recrystallization (DDRX) and continuous dynamic recrystallization (CDRX).^[1,42] DDRX is characterized by nucleation and growth of new grains and occurs mainly in materials with low stacking fault energy.^[43] As nucleation occurs preferentially at defects, such as grains boundaries, a necklace microstructure often characterizes this type of recrystallization, the large initial grains being surrounded by smaller recrystallized grains.^[44] On the other hand, CDRX occurs by progressive transformation of low angle boundaries (LABs) into high angle boundaries (HABs) and it is

promoted in materials with high stacking fault energy. It can be noted that a third type of dynamic recrystallization has been identified, the geometric dynamic recrystallization (GDRX), which corresponds to the formation of a new grain structure resulting from a change in grain geometry in high stacking fault materials.^[43] Alloy 718 having a relatively low stacking fault energy (in the order of 10⁻² J/m²^[45]), its deformation behavior at high temperature is expected to be dominated by DDRX,^[44] but studies of the deformation behavior of alloy 718 at low strain rates have shown that both DDRX and CDRX take place in the material.^[10–12,16]

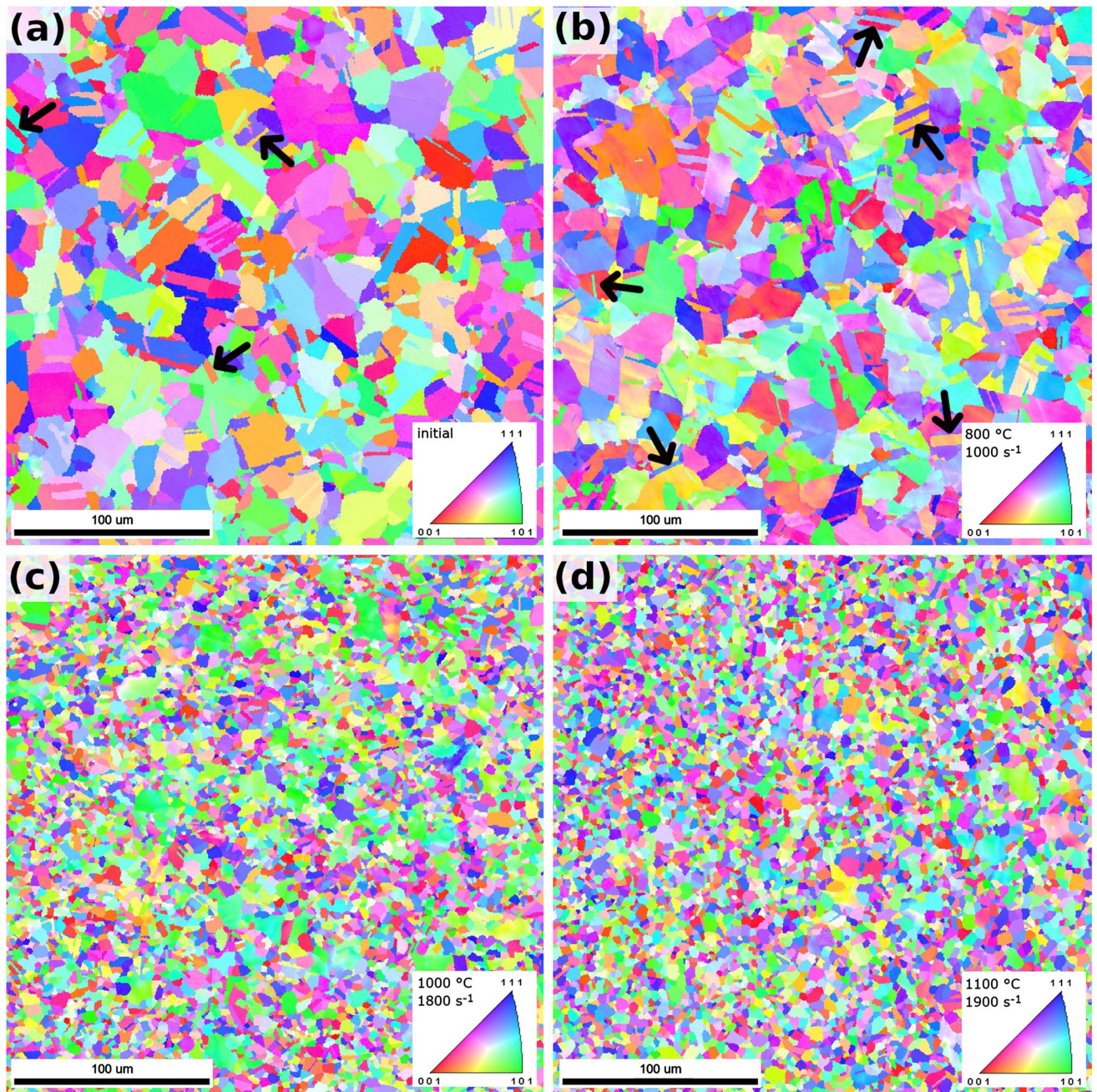


Fig. 9—Inverse Pole Figures (IPF) obtained by EBSD analysis of alloy 718 in aged state (a) initial material (b) deformed at 800 °C (c) deformed at 1000 °C (d) deformed at 1100 °C (strain rate between 1000 s⁻¹ and 1900 s⁻¹)—black arrows indicate twins (Color figure online).

Considering the mechanical results and the microstructural analysis, evidence for the occurrence of recrystallization, both dynamic and meta-dynamic, are provided and it is then discussed whether this recrystallization is discontinuous or continuous. In addition, the equiaxed grains of the initial microstructure of both annealed and aged materials (Figure 4) indicate that the as-received materials were relieved of stress and internal stored energy during a previous heat-treatment process. So static recrystallization cannot occur during heating of the sample^[42] and instead,

dynamic and meta-dynamic recrystallization were initiated due to deformation at high temperature.

Evidence for recrystallization Recrystallization usually leads to a very typical flow stress behavior, for which the decrease in stress is visible on the stress–strain curves. In the current study, such a softening stage is not clearly visible on the curves of Figures 5 through 7, but a relative softening is observed for the highest temperatures, 1000 °C and 1100 °C. As previously mentioned, the recrystallization is thought to initiate during the deformation and to continue after removal of external

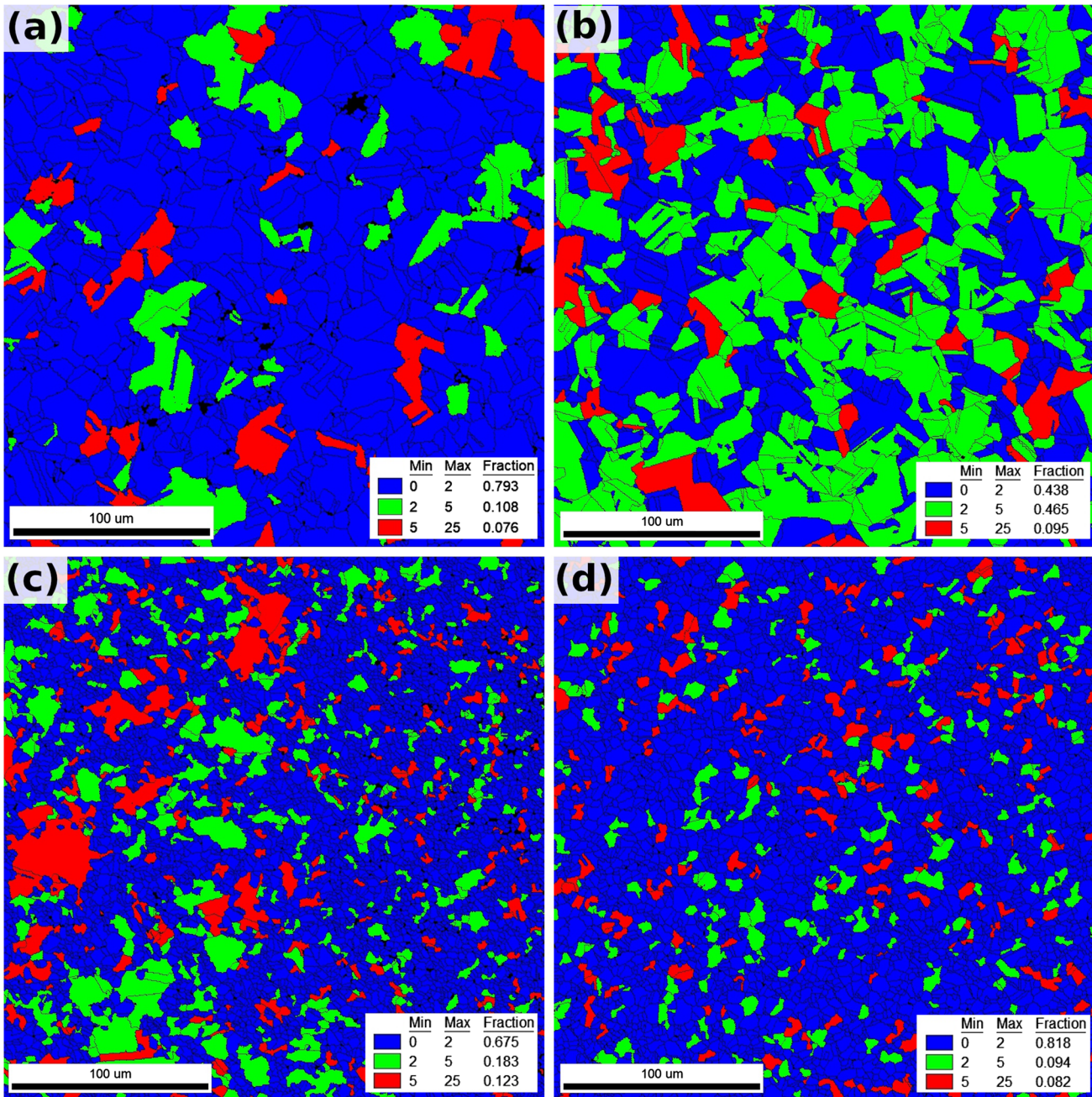


Fig. 10—Grain Orientation Spread (GOS) maps obtained by EBSD analysis of alloy 718 in annealed state (a) initial material (b) deformed at 800 °C (c) deformed at 1000 °C (d) deformed at 1100 °C (strain rate between 1300 s⁻¹ and 1800 s⁻¹) (Color figure online).

forces. Then, only the initiation of the recrystallization mechanism can be observed on the stress–strain curves, explaining the lack of a clear softening stage. The microstructural characterization using EBSD, Figures 8 through 12, shows that new small grains are formed when the material is deformed at 1000 °C and 1100 °C, and that those grains exhibit low plastic deformation. It can be deduced that they are recrystallized. On the other hand, the large deformed grains observed at 1000 °C correspond to the grains inherited from the initial microstructure. For further discussion, quantification of boundary rotation, misorientation angle and grain

size distribution in the material was performed, as displayed in Figures 13 and 14 for the aged material. LABs have a boundary rotation angle and a misorientation angle below 15 ° and they appear in red and green in the grain boundary rotation maps. HABs have a boundary rotation angle and a misorientation angle above 15 ° and they correspond to the blue lines in the grain boundary rotation maps. For both annealed and aged state, the material deformed at 1000 °C and 1100 °C presents a larger proportion of HABs compared to the initial material and the one deformed at 800 °C. Figure 13 shows that, for the aged state, there is around

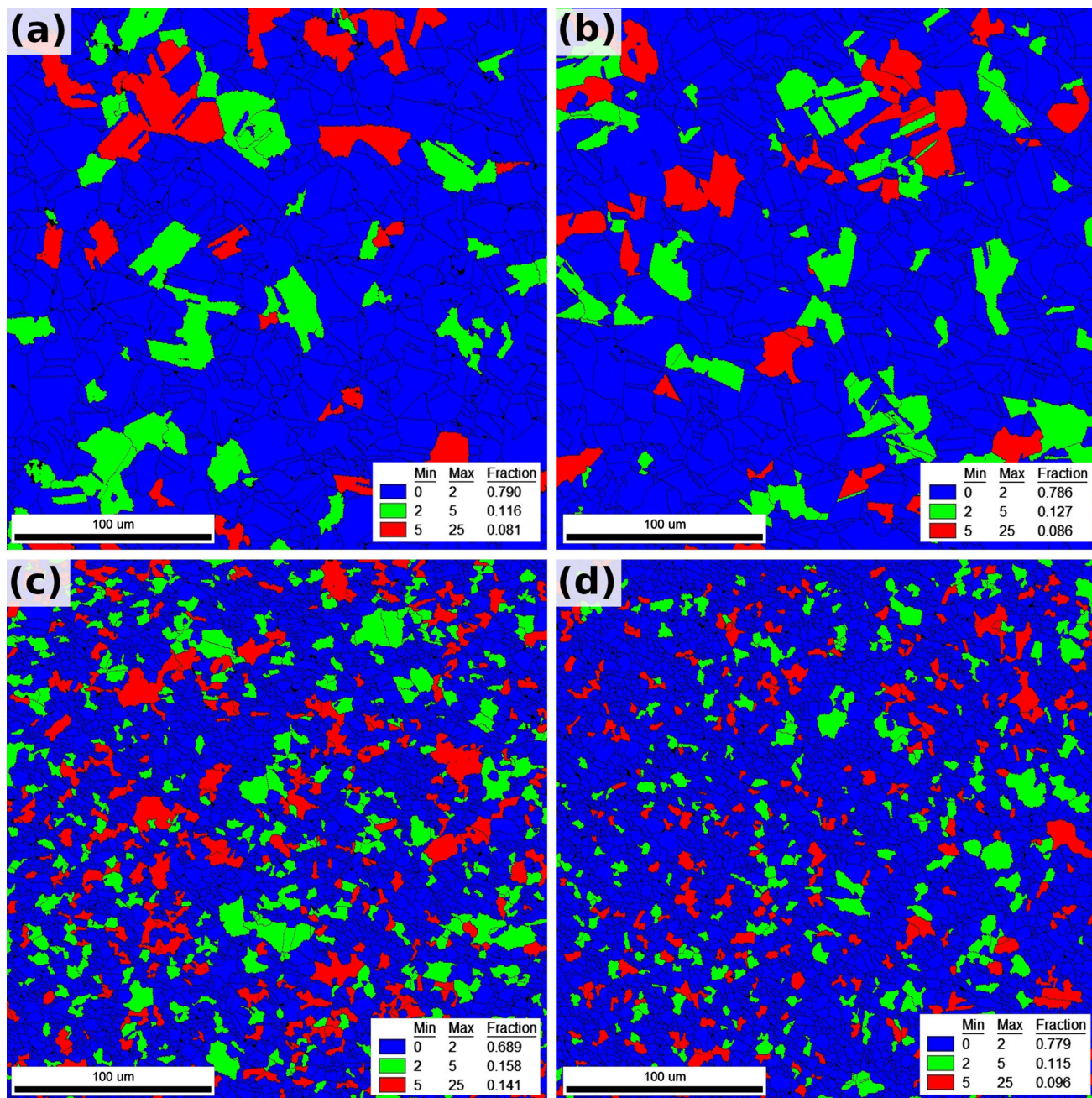


Fig. 11—Grain Orientation Spread (GOS) maps obtained by EBSD analysis of alloy 718 in aged state (a) initial material (b) deformed at 800 °C (c) deformed at 1000 °C (d) deformed at 1100 °C (strain rate between 1000 and 1900 s⁻¹) (Color figure online).

35 pct of HABs in the initial material, 40 pct in the material deformed at 800 °C, 65 pct in the material deformed at 1000 °C and 70 pct in the material deformed at 1100 °C. The proportion of twin boundaries, which correspond to misorientation angles of around 60 deg around $\langle 111 \rangle$ axis, is decreased significantly in the material deformed at 1000 °C and 1100 °C, compared to the initial state. Figure 14(a) displays that, for the aged material, there is around 45 pct of twin boundaries in the initial material, 30 pct in the material deformed at 1000 °C and 20 pct in the material deformed at 1100 °C. In addition, the grain size

distribution presented in Figure 14(b) shows that, after deformation at 1000 °C and 1100 °C, the material contains mainly small grains below 5 μm, whereas the average grain size for the initial material is approximately 15 μm. All these observations indicate that recrystallization took place when the material was deformed at 1000 °C and 1100 °C, through removing of the old grains and twins, which are replaced by a refined and defect-free microstructure. It must be noted that a comparison between the material deformed at 1000 °C and the one deformed at 1100 °C is not possible with the EBSD data only, as, for 1000 °C, they are not

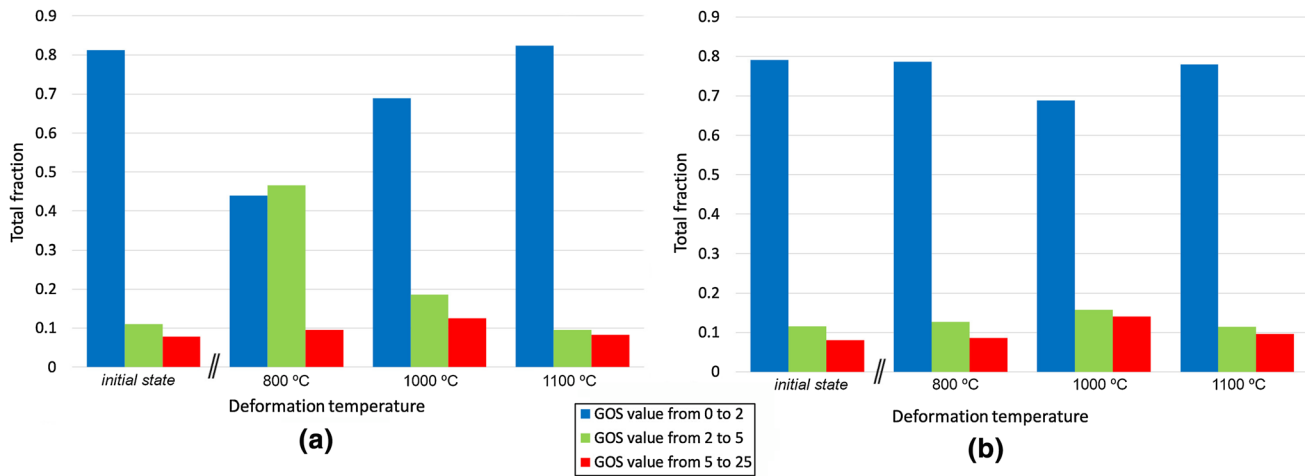


Fig. 12—Grain Orientation Spread (GOS) distribution obtained by EBSD analysis of alloy 718 (a) in annealed state (b) in aged state corresponding to Figs. 10 and 11, respectively (Color figure online).

representative of the entire sample, which presents a very inhomogeneous recrystallization. This is further discussed in the next Section IV–B.

Discontinuous or continuous recrystallization? As mentioned in Section III–C, very small grains were observed in the microstructure of the material deformed at 1000 °C. Those grains are located at defects, like grain boundaries, as shown in Figure 15. Necklace structures are clearly visible, as indicated within the black frames in Figures 15(b) and (c). This indicates that new grains nucleate at defects and grain boundaries, thus establishing the occurrence of discontinuous recrystallization.^[43,46] Therefore, it appears that recrystallization occurred mainly through discontinuous mechanisms, especially at the first stages of recrystallization. However, continuous recrystallization probably also takes place, as it has been observed for deformation at low strain rates.^[10–12]

B. Effect of Deformation Temperature

Occurrence of recrystallization in a material depends on the temperature, as well as material parameters, strain and strain rate. For alloy 718, recrystallization has been observed above 900 °C for low strain rates.^[10–14] In the current study, similar results have been observed for high strain rates: for the material deformed at 800 °C, recrystallization did not occur at all, whereas a significant amount of recrystallized grains was identified in the material deformed at 1000 °C and above.

For a deformation temperature of 1000 °C, it appears that only partial recrystallization took place. As previously mentioned in Section III–C, the grain size is highly non-homogeneous and Figure 15 highlights that different zones of the same section of a sample present different recrystallization stages. In some areas, the recrystallization has not started and the initial grains ($\sim 15 \mu\text{m}$) and twins (indicated by the black arrows in Figure 15(a)) are observed. In the “transition” zones, both recrystallized grains and initial grains are found

and the twin boundaries are disappearing (Figure 15(b)), indicating that the recrystallization has started but is not completed. Finally, some areas, where the grain size is homogeneous and smaller than the initial one, appear to be mostly recrystallized (Figure 15(c)). On the other hand, after deformation at 1100 °C, the material is mostly recrystallized, with an homogeneous recrystallized grain size. Similar observations were made by Krawczyk *et al.*^[2] in forging conditions.

Furthermore, microstructural analysis of the material deformed at higher strain rate than previously discussed (around 2400 s^{-1}) are presented in Figure 16 for the annealed material and in Figure 17 for the aged material. These images show that the average recrystallized grain size is larger for the material deformed at 1100 °C, suggesting that the recrystallized grains grow to a larger extent during deformation at higher temperature and strain rate (1100 °C and 2400 s^{-1}).

It is, therefore, concluded that the material deformed at 1100 °C presents a more advanced stage of recrystallization than the one deformed at 1000 °C. At 1000 °C, the recrystallized grains just started to nucleate in some areas of the sample, the material being only partially recrystallized. However, at 1100 °C, the material is fully recrystallized and the thermally-activated diffusion mechanism is more active, so growth of the recrystallized grains was promoted. Considering that, at a constant strain rate, the time for all the compression tests is similar, it was concluded that, during deformation at high strain rate of alloy 718, recrystallization kinetics increases with increasing temperature.

C. Influence of Initial Heat Treatment

Depending on the initial heat treatment, the material contains different types and amounts of precipitates, and exhibits a different mechanical behavior. From the mechanical results presented in Section III–B, it was deduced that the aged material undergoes at least a

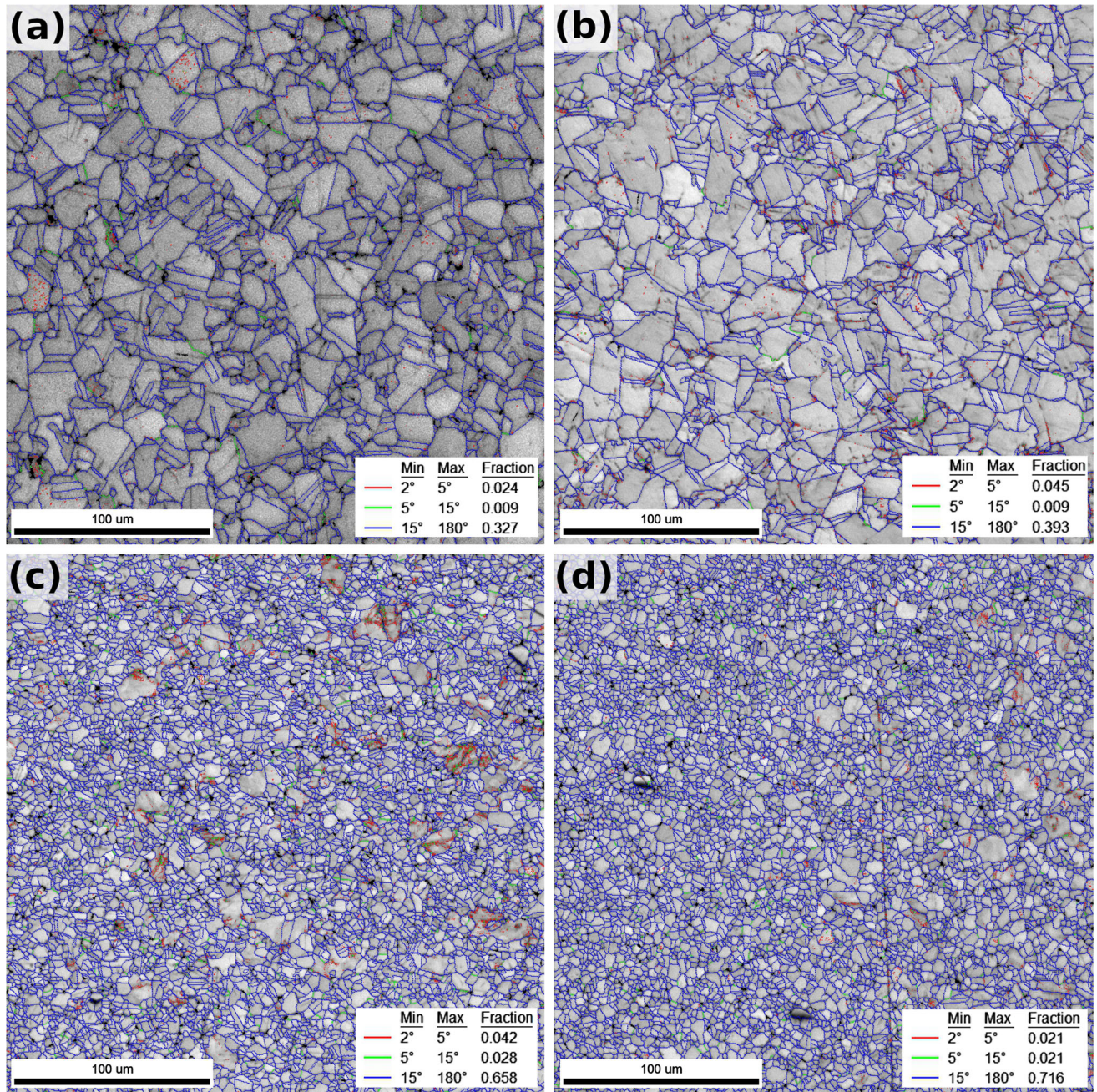


Fig. 13—Grain boundary rotation maps obtained by EBSD analysis of alloy 718 in aged state (a) initial material (b) deformed at 800 °C (c) deformed at 1000 °C (d) deformed at 1100 °C (strain rate between 1000 and 1900 s⁻¹) (Color figure online).

partial dissolution of its precipitates when heated and deformed at 1000 °C and above. Figure 18 supports this observation, as a sudden drop in the yield strength can be observed in the aged material for deformation at 1000 °C and above. However, it can be noted that, even for those temperatures, the aged material still exhibits a slightly higher yield strength than the annealed one, suggesting that the dissolution of precipitates is not completed. This could be explained by the short duration for which the sample is exposed to temperatures above 950 °C (around 20 seconds, see Figure 3). The microstructural characterization, presented in

Section III-C and further supported by Figures 16 and 17, suggests that the initial heat treatment does not affect the recrystallized microstructure to a great extent. Even so, it seems that, after deformation at 1100 °C and higher strain rate (2400 s⁻¹), the recrystallized grains are larger in the annealed material. In Figures 16(b) and 17(b), the average grain size is 8.8 μm for the annealed material and 7.6 μm for the aged material. This could mean that the remaining precipitates in the aged material deformed at 1100 °C impede grain growth to some extent, by pinning of grain boundaries.^[6,47] Another possible explanation is related to the total

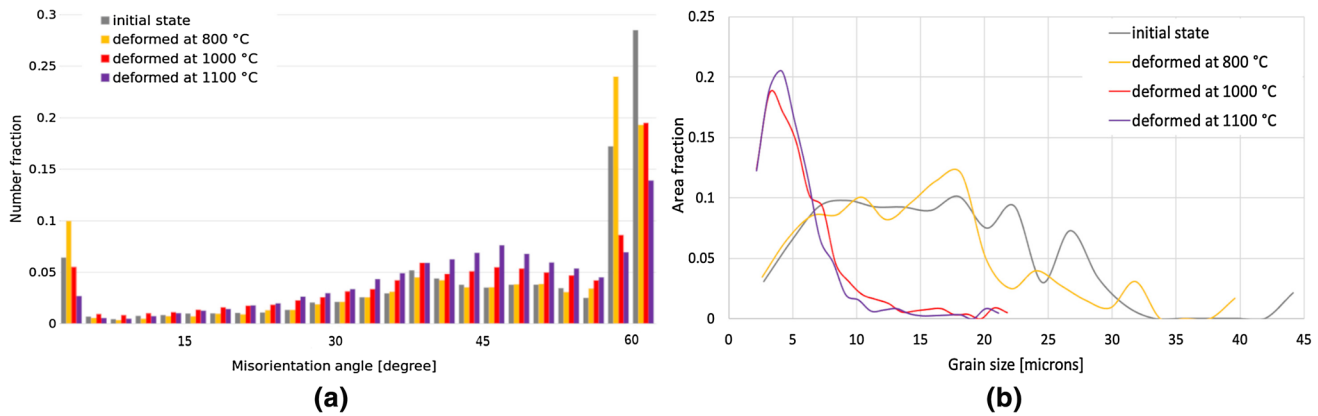


Fig. 14—(a) Misorientation angle distribution and (b) grain size distribution obtained by EBSD analysis of alloy 718 in aged state corresponding to Figure 13 (Color figure online).

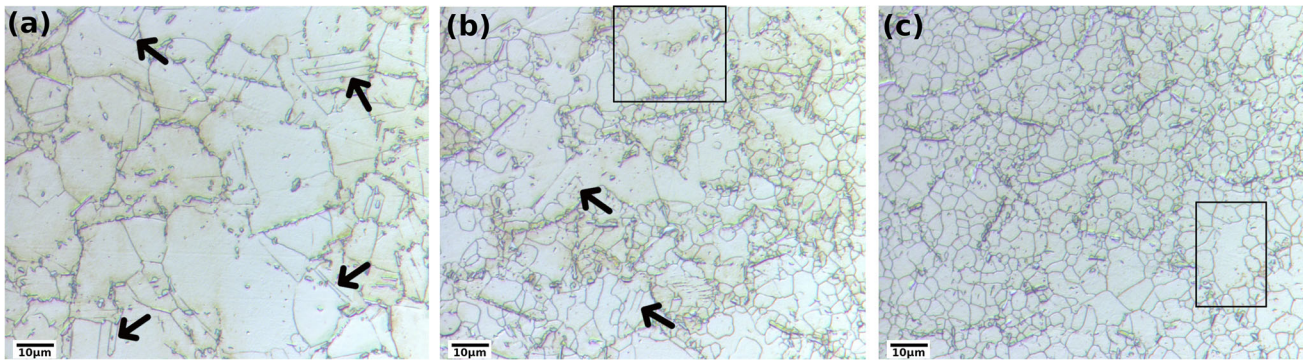


Fig. 15—Optical micrographs of alloy 718 in annealed state deformed at 1000 °C and 1800 s⁻¹ for three different zones in the same sample: (a) non-recrystallized (b) partially recrystallized (c) mostly recrystallized—black arrows indicate twins—black frames show necklace structures.

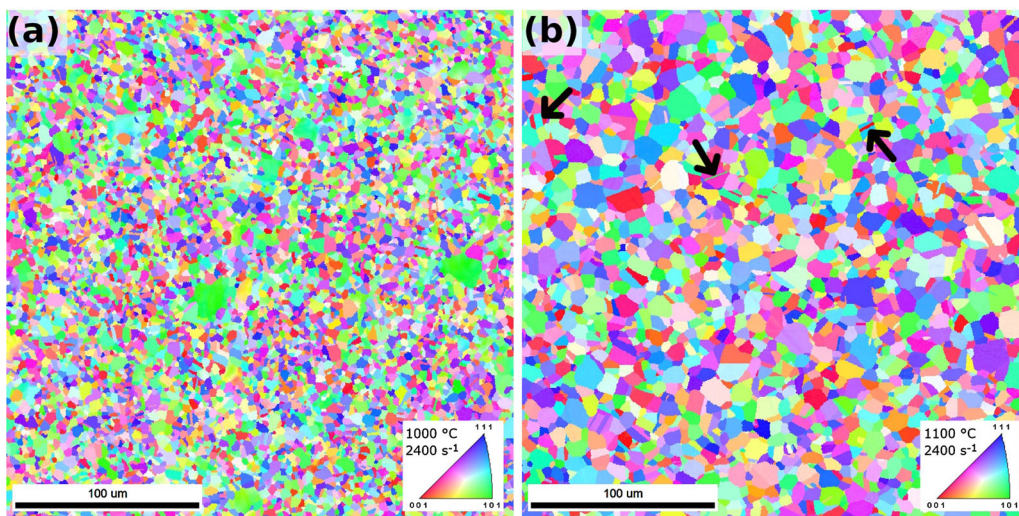


Fig. 16—Inverse Pole Figures (IPF) obtained by EBSD analysis of alloy 718 in annealed state (a) deformed at 1000 °C and 2400 s⁻¹ (b) deformed at 1100 °C and 2400 s⁻¹—black arrows indicate twins (Color figure online).

strain. The annealed material being more prone to deformation than the aged one, it accumulates more strain and internal energy (as it is suggested by the stress–strain curves in Figure 7), thus increasing the dislocation density and promoting recrystallization.

D. Influence of Strain Rate

Considering the mechanical results presented in Section III–B, the effect of strain rate appears not to be significant for the recrystallization conditions (1000 °C

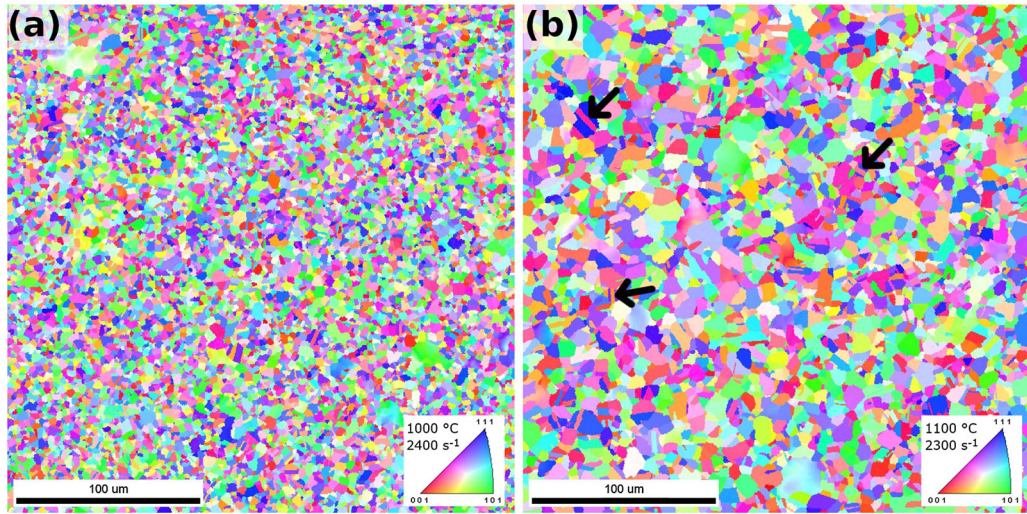


Fig. 17—Inverse Pole Figures (IPF) obtained by EBSD analysis of alloy 718 in aged state (a) deformed at 1000 °C and 2400 s⁻¹ (b) deformed at 1100 °C and 2300 s⁻¹—black arrows indicate twins (Color figure online).

and 1100 °C). However, the microstructural analysis of the material deformed at 1100 °C suggests that the recrystallized grain size at this temperature increases with the strain rate. For the annealed state, Figures 8(d) and 16(b), the average recrystallized grain size is 5.3 μm when deformed at 1500 s⁻¹ and 8.8 μm when deformed at 2400 s⁻¹. For the aged state, Figures 9(d) and 17(b), the average recrystallized grain size is 5.3 μm when deformed at 1900 s⁻¹ and 7.6 μm when deformed at 2300 s⁻¹. Tan *et al.*^[14] have made similar observations in the low strain rate domain. It was also noted that the samples deformed at 1000 °C and 1100 °C tend to be more recrystallized when deformed at higher strain rate, for both states. This observation is consistent with the studies made by Zhou and Baker^[48] for low strain rates and Iturbe *et al.*^[18] for medium strain rates, where it was observed that increasing the strain rate leads to a higher proportion of recrystallized grains. These results could be explained by the conclusions made by Guest and Tin.^[40] They observed that, although a higher strain rate leads to a lower volume of recrystallized grains during the deformation (dynamic recrystallization), the

meta-dynamic recrystallization rate is higher for a higher strain rate. They explained it by a higher adiabatic heating of the sample, as well as the limitation of recovery, which allows a greater dislocation density accumulation, thus higher driving force for the recrystallization. In any case, the effect of strain rate on the combined dynamic and meta-dynamic recrystallization is complex, as it affects those mechanisms in a different way and as it is intertwined with the effect of temperature (adiabatic heating). In addition, others factors have to be taken into account when investigating its effect, such as the variation of strain rate during the test, the non-homogeneous recrystallization and the quantification of grain size only on specific areas. Nevertheless, the strain rate has much less effect on the deformation behavior than the temperature.

V. CONCLUSION

The behavior of alloy 718 in annealed and aged states at high strain rates and high temperatures has been characterized using Split-Hopkinson pressure bar, OM and SEM. It has been observed and deduced the following:

- The flow stress decreases with increasing temperature and decreasing strain rate, which is the common behavior of metals and alloys.
- For deformation temperatures below 1000 °C, the aged material presents a yield strength approximately 200 MPa higher than the annealed material. It is also more resistant to deformation, with only 20 pct of the grains being deformed after compression at 800 °C, against more than 50 pct for the annealed material. However, at 1100 °C, the difference in yield strength between the two states decreases significantly and the flow stress level of both states are similar, suggesting a dissolution of the strengthening precipitates in the aged material.

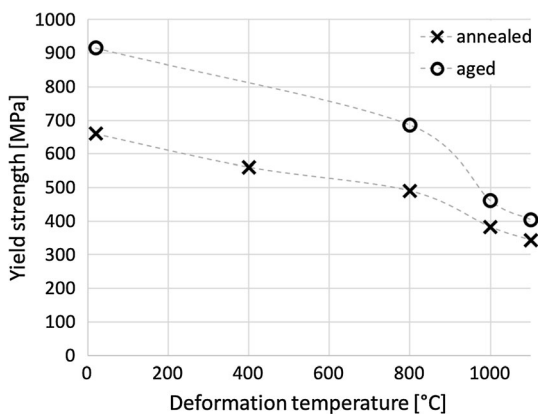


Fig. 18—Yield strength vs temperature for alloy 718 in annealed and aged states.

- Recrystallization (DRX and MDRX) takes place in both annealed and aged alloy 718 when deformed at 1000 °C and 1100 °C, leading to refinement of the microstructure.
- Discontinuous recrystallization (or DDRX) was identified as the main recrystallization mechanism, via the formation of necklace structures.
- Recrystallization kinetics increases with increasing temperature, meaning that a higher deformation temperature leads to a higher fraction of recrystallized grains and a larger recrystallized grain size. Deformation at 1000 °C generates an incomplete recrystallization, whereas deformation at 1100 °C results in a fully recrystallized microstructure.

The current study gives a better understanding of alloy 718 deformation behavior at high strain rates and high temperatures, conditions which have seldom been studied in the literature. This work aims at improving modelling of the microstructural evolution, including recrystallization, in this alloy, and it will be used to better predict the final mechanical and microstructural state of the material during and after manufacturing processes.

ACKNOWLEDGMENTS

This research work is a part of the European Network for Alloys behaviour Laws Enhancement (ENABLE) project funded by the European Union's Marie Skłodowska-Curie Actions (MSCA) Innovative Training Networks (ITN) H2020-MSCA-ITN-2017 under the grant agreement N°764979. The authors gratefully acknowledge Sandvik Coromant for providing the material used in this study. The authors would also like to thank the Centre des Matériaux of MINES ParisTech (France) for providing access to their laboratories, as well as for the help received when using the equipment. Finally, the authors would like to thank professor Frank Montheillet, MINES Saint-Étienne, for valuable discussion on recrystallization in metals, and professor Loïc Nazé, MINES ParisTech, for his helpful explanation and comments regarding alloy 718 microstructure.

FUNDING

Open access funding provided by Lulea University of Technology.

OPEN ACCESS

This article is licensed under a Creative Commons Attribution 4.0 International License, which permits use, sharing, adaptation, distribution and reproduction in any medium or format, as long as you give appropriate credit to the original author(s) and the source, provide a link to the Creative Commons licence, and indicate if changes were made. The images or other third party material in this article are included in the

article's Creative Commons licence, unless indicated otherwise in a credit line to the material. If material is not included in the article's Creative Commons licence and your intended use is not permitted by statutory regulation or exceeds the permitted use, you will need to obtain permission directly from the copyright holder. To view a copy of this licence, visit <http://creativecommons.org/licenses/by/4.0/>.

CONFLICT OF INTEREST

The authors declare that they have no conflict of interest.

REFERENCES

1. R.D. Doherty, D.A. Hughes, F.J. Humphreys, J.J. Jonas, D. Juul Jensen, M.E. Kassner, W.E. King, T.R. McNelley, H.J. McQueen, and A.D. Rollett: *Mater. Sci. Eng. A*, 1997, vol. 238, pp. 219–74.
2. A. Krawczyk, A. Łukaszek-Sołek, T. Śleboda, P. Bała, S. Bednarek, and M. Wojtaszek: *Archiv. Metall. Mater.*, 2012, vol. 57, pp. 593–603.
3. Y.S. Na, J.T. Yeom, N.K. Park, and J.Y. Lee: *Metals Mater. Int.*, 2003, vol. 9, pp. 15–19.
4. R. Damodaram, S.G.S. Raman, and K.P. Rao: *Mater. Sci. Eng. A*, 2013, vol. 560, pp. 781–86.
5. F.C. Liu and T.W. Nelson: *Mater. Charact.*, 2018, vol. 140, pp. 39–44.
6. P.C. Yadav, S. Sahu, A. Subramaniam, and S. Shekhar: *Mater. Sci. Eng. A*, 2018, vol. 715, pp. 295–306.
7. X.P. Ren and Z.Q. Liu: *Int. J. Miner. Metall. Mater.*, 2018, vol. 25, pp. 937–49.
8. F. Jafarian, S. Masoudi, H. Soleimani, and D. Umbrello: *Mater. Manuf. Process.*, 2018, vol. 33, pp. 1020–29.
9. M. Azarbarmas, M. Aghaie-Khafri, J.M. Cabrera, and J. Calvo: *Mater. Des.*, 2016, vol. 94, pp. 28–38.
10. M. Azarbarmas, M. Aghaie-Khafri, J.M. Cabrera, and J. Calvo: *Mater. Sci. Eng. A*, 2016, vol. 678, pp. 137–52.
11. Y. Wang, W.Z. Shao, L. Zhen, and X.M. Zhang: *Mater. Sci. Eng. A*, 2008, vol. 486, pp. 321–32.
12. F. Montheillet, J.P. Thomas, In: *Metallic Materials with High Structural Efficiency*, ed. by O.N. Senkov, D.B. Miracle, S.A. Firstov, Kluwer Academic Publishers, pp. 357–68 (2004).
13. F.L. Sui, L.X. Xu, L.Q. Chen, and X.H. Liu: *J. Mater. Process. Technol.*, 2011, vol. 211, pp. 433–40.
14. Y.B. Tan, Y.H. Ma, and F. Zhao: *J. Alloys Compd.*, 2018, vol. 741, pp. 85–96.
15. F. Chen, J. Liu, H. Ou, B. Lu, Z. Cui, and H. Long: *Mater. Sci. Eng. A*, 2015, vol. 642, pp. 279–87.
16. J.P. Thomas, E. Bauchet, C. Dumont, and F. Montheillet: *Proceedings of the International Symposium on Superalloys*, 2004, pp. 959–68.
17. H. Yuan and W.C. Liu: *Mater. Sci. Eng. A*, 2005, vol. 408, pp. 281–89.
18. A. Iturbe, E. Giraud, E. Hormaetxe, A. Garay, G. Germain, K. Ostolaza, and P.J. Arrazola: *Mater. Sci. Eng. A*, 2017, vol. 682, pp. 441–53.
19. W.S. Lee, C.F. Lin, T.H. Chen, and H.W. Chen: *Mater. Sci. Eng. A*, 2011, vol. 528, pp. 6279–86.
20. W.S. Lee, C.F. Lin, T.H. Chen, and H.W. Chen: *Mater. Trans.*, 2011, vol. 52, pp. 1734–40.
21. W.S. Lee, C.F. Lin, T.H. Chen, and C.S. Huang: *Mater. Trans.*, 2012, vol. 53, pp. 1758–64.
22. X. Wang, C. Huang, B. Zou, H. Liu, H. Zhu, and J. Wang: *Mater. Sci. Eng. A*, 2013, vol. 580, pp. 385–90.
23. T. Sjöberg, K.G. Sundin, M. Oldenburg, in *Computational Plasticity XII: Fundamentals and Applications*. COMPLAS , pp. 790–800 (2013).
24. T. Sjöberg, J. Kajberg, and M. Oldenburg: *Eng. Fract. Mech.*, 2017, vol. 178, pp. 231–42.

25. J. Johansson, C. Persson, H. Lai, and M. Hörnqvist Colliander: *Mater. Sci. Eng. A*, 2016, vol. 662, pp. 363–72.
26. L.Y. Wei, S. Azadian, R. Warren, K. Wei, In: 52nd annual meeting on Scandinavian Society for Electron Microscopy, pp. 208–09 (2001).
27. J.M. Pereira and B.A. Lerch: *Int. J. Impact Eng.*, 2001, vol. 25, pp. 715–33.
28. Special Metals. INCONEL alloy 718 Datasheet 2007.
29. Maher. *Alloy 718 Data Sheet* (2020).
30. J. Kajberg and K.G. Sundin: *J. Mater. Process. Technol.*, 2013, vol. 213, pp. 522–31.
31. G.T. Gray, ASM Handbook **8**, 462–76 (2000).
32. J.I. Goldstein, D.E. Newbury, J.R. Michael, N.W. Ritchie, J.H.J. Scott, and D.C. Joy: *Scanning Electron Microscopy and X-Ray Microanalysis*, 4th ed., Springer, New York, 2017.
33. M. Urdanpilleta, J.M. Martínez-Esnaola, and J.G. Sevillano: *Mater. Trans.*, 2005, vol. 46, pp. 1711–19.
34. S.L. Yan, H. Yang, H.W. Li, and X. Yao: *J. Alloys Compd.*, 2016, vol. 688, pp. 776–86.
35. S. Azadian, Aspects of Precipitation in the Alloy Inconel 718. (Luleå University of Technology). (Ph.D. thesis) (2004).
36. M. Fisk, J.C. Ion, and L.E. Lindgren: *Comput. Mater. Sci.*, 2014, vol. 82, pp. 531–39.
37. G. Asala, J. Andersson, and O.A. Ojo: *Philos. Mag.*, 2019, vol. 99, pp. 419–37.
38. S.I. Wright, M.M. Nowell, and D.P. Field: *Micros. Microanal.*, 2011, vol. 17, pp. 316–29.
39. J.J. Jonas: *Mater. Sci. Eng. A*, 1994, vol. 184, pp. 155–65.
40. R.P. Guest, S. Tin, In: Proceedings of the International Symposium on Superalloys and Various Derivatives, pp. 373–83 (2005).
41. A. Nicolaÿ, J.M. Franchet, J. Cormier, H. Mansour, M. de Graef, A. Seret, and N. Bozzolo: *J. Microsc.*, 2019, vol. 273, pp. 135–47.
42. F. Montheillet, In: *Moving Interfaces in Crystalline Solids*. ed. by F.D. Fischer, Springer, New York, pp. 203–56 (2004).
43. K. Huang and R. Logé: *Mater. Des.*, 2016, vol. 111, pp. 548–74.
44. F. Montheillet: *Techniques de l'Ingenieur - M3031* (2009).
45. M. Sundararaman, P. Mukhopadhyay, and S. Banerjee: *Acta Metall.*, 1988, vol. 36, pp. 847–64.
46. D. Ponge and G. Gottstein: *Acta Mater.*, 1998, vol. 46, pp. 69–80.
47. H.T. Lee and W.H. Hou: *Mater. Sci. Eng. A*, 2012, vol. 555, pp. 13–20.
48. L.X. Zhou and T.N. Baker: *Mater. Sci. Eng. A*, 1994, vol. 177, pp. 1–9.

Publisher's Note Springer Nature remains neutral with regard to jurisdictional claims in published maps and institutional affiliations.